

Acoustic emissions analysis of damage in amorphous and crystalline metal foams

A.H. Brothers^a, D.W. Prine^b, D.C. Dunand^{a,*}

^a Department of Materials Science and Engineering, Northwestern University, Evanston, IL 60208, USA

^b Infrastructure Technology Institute, Northwestern University, Evanston, IL 60208, USA

Available online 2 March 2006

Abstract

Acoustic emission methods are used to investigate the nature and evolution of microfracture damage during uniaxial compression of ductile amorphous and brittle crystalline metal foams made from a commercial Zr-based bulk metallic glass, and to compare this behavior against that of aluminum-based foam of similar structure. For the amorphous foam, acoustic activity reveals evolution of the damage process from diffuse to localized damage through the foam stress plateau region, and reversion back towards diffuse damage in the foam densification region. Accommodation of microfracture by surrounding ductile struts, and significant point contact formation, permit high average compressive strains of ca. 80% in the amorphous foam without macroscopic failure.

© 2006 Elsevier Ltd. All rights reserved.

Keywords: B. Brittleness and ductility; B. Glasses, metallic; F. Mechanical testing

1. Introduction

Metallic foams are recognized for their potential as structural materials, due to their high density-compensated strength and stiffness, mechanical energy absorption and acoustic damping [1,2]. This interest in structural applications has motivated investigation of amorphous metals as alternatives to conventional crystalline metals in foam architectures, on account of their high-strength (typically around 2 GPa in compression [3], though amorphous alloys having compressive strengths above 5 GPa have been reported [4]), corrosion resistance, and processability (low liquidus temperatures in comparison to crystalline metals of similar strength, and high viscosity allowing foaming in the supercooled liquid state [5,6]). In order for amorphous metal foams to be viable alternatives to crystalline metal foams, however, it is necessary for them to exhibit compressive ductility far in excess of monolithic amorphous metals, which are typically limited to less than 1% compressive plastic strain in the absence of geometric confinement [7], ductile reinforcement [8], or anomalously-high Poisson's ratios [9]. At low to intermediate porosities (< 70%), some ductility can be achieved by interruption of shear band motion through intersection with pores, and by tortuosity

in shear band paths associated with the highly non-uniform local stress environments around pores [10–12]. In less-dense, cellular foam architectures (> 70% porosity), compressive ductility is further improved by stable shear band extension in slender struts subjected locally to bending [7,13,14].

Effectively maximizing ductility in amorphous metal foams requires, however, detailed understanding of internal deformation and damage mechanisms. Significant damage accumulation in low-density amorphous metal foams has been previously reported and is evident through serrations on their stress–strain curves and a decrease in stiffness with increasing plastic deformation [14]. In this report, we investigate the nature of this damage using acoustic emissions (AE) analysis, which has proven useful in the study of similar fracture processes in monolithic and composite materials [15] as well as porous rocks [16], cellular ceramics [17], and more recently low-density crystalline metallic foams [18].

Through analysis of AE activity generated by internal microfracture, it is shown here that deformation in amorphous metal foams involves substantial damage (relative to ductile Al–Si foam), and that this damage resembles, in its AE signature, microfracture damage within brittle ceramic foams (including devitrified amorphous metal foam). Nonetheless, stabilizing mechanisms are active in the amorphous metal foam which allow high average compressive strains (ca. 80%) without final failure, so that macroscopically their compressive behavior is hardly distinguishable from that of ductile crystalline metal foams.

* Corresponding author. Tel.: +1 847 491 5370; fax: +1 847 491 7820.

E-mail address: dunand@northwestern.edu (D.C. Dunand).

2. Materials and methods

Foam samples were processed from the bulk metallic glass-forming alloy Vit106 ($Zr_{57}Nb_5Cu_{15.4}Ni_{12.6}Al_{10}$; here and elsewhere, compositions are given in at.%) using the salt replication method, described in further detail previously [13,19]. Pre-alloyed buttons of Vit106 were prepared by arc melting high-purity ($\geq 99.5\%$) metals several times under a Ti-gettered argon atmosphere, followed by vacuum remelting and quenching in stainless steel crucibles. Charges of Vit106 were then melted and pressure infiltrated ($975\text{ }^\circ\text{C}$, 156 kPa total pressure gradient of high-purity argon gas in stainless steel crucibles) into 6 mm diameter cylindrical patterns of high-purity BaF_2 salt produced by vacuum sintering ($1250\text{ }^\circ\text{C}$, 10 h). After quenching, infiltrated patterns were machined into uniform cylinders using a diamond grinding wheel and diamond wafering saw and immersed in ultrasonically-agitated 2 M HNO_3 solution near $50\text{ }^\circ\text{C}$ to dissolve the BaF_2 and to thin the remaining Vit106 struts to a predetermined foam density, as determined by dry mass and dimensions.

A Vit106 foam sample processed using a BaF_2 pattern of $150\text{--}212\text{ }\mu\text{m}$ particle size with final relative density 24%, machined to a diameter 3.5 mm and height of 7.6 mm, was selected for AE analysis; its fully amorphous state was verified by Cu $K\alpha$ X-ray diffraction before and after testing (Fig. 1a). A second amorphous Vit106 sample, processed from a BaF_2 pattern of $300\text{--}355\text{ }\mu\text{m}$ particle size with final density 17%, diameter 3.9 mm, and height 5.7 mm, was vacuum annealed at $450\text{ }^\circ\text{C}$ for 3 h to induce near-complete crystallization, in accordance with the Vit106 TTT diagram [20,21]. The sample dimensions were remeasured after annealing to ascertain that no dimensional changes associated with viscous flow occurred during annealing in the supercooled liquid region. The foam was examined after compression by X-ray diffraction to confirm crystallization (Fig. 1b). In addition, a pure aluminum foam of comparable dimensions to the other specimens (3.9 mm diameter, 7.9 mm height, relative density 28%) was

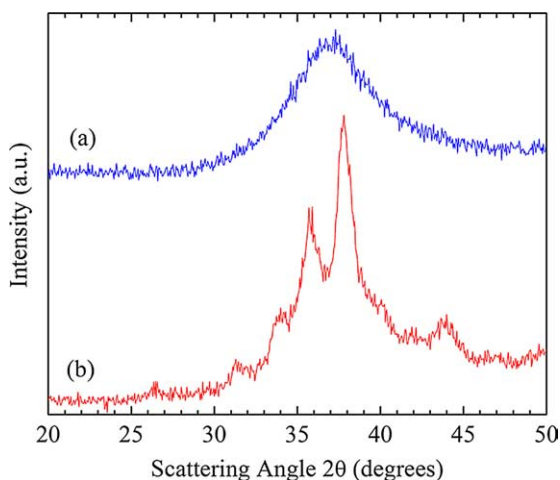


Fig. 1. X-ray diffraction patterns taken from deformed samples of (a) amorphous Vit106 foam; and (b) crystalline Vit106 foam prepared by devitrifying an amorphous sample.

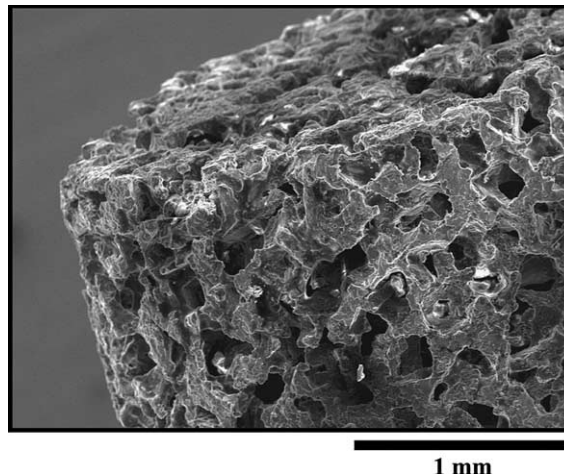


Fig. 2. Scanning electron micrograph showing a representative salt-replicated foam structure (in this case, eutectic Al–Si). The pore size and relative density of this foam were $150\text{--}212\text{ }\mu\text{m}$ and 42%, respectively.

made by infiltration and dissolution of NaCl patterns prepared from ca. $500\text{ }\mu\text{m}$ NaCl powders. Finally, eutectic Al–Si (approx. Al–12.6 wt% Si) foam (3.5 mm diameter, 7.7 mm height, relative density 42%) was produced by replication of $150\text{--}212\text{ }\mu\text{m}$ NaCl powders. A scanning electron micrograph (Hitachi S-3500N) of this Al–Si foam is shown in Fig. 2; the structure of this sample was very similar to the structure of other (i.e. pure aluminum and Vit106) samples and is broadly representative of replicated foams, showing high uniformity in density and pore size and pronounced ‘nodes’ at the intersections of its struts [14,22,23].

Quasi-static uniaxial compression was performed on all samples using a displacement-controlled screw-driven load frame (Fig. 3). A nominal strain rate of $5 \times 10^{-4}\text{ s}^{-1}$ was used everywhere, except that higher anticipated acoustic event rates motivated the choice of a lower strain rate of 10^{-4} s^{-1} for crystalline Vit106. To account for this difference, acoustic data are presented as events per unit strain, rather than per unit time. Compression was applied using hardened tool steel pistons with a lubricated steel sleeve ensuring parallelism, and average foam strain was determined from crosshead displacement after correction for load-train compliance using calibration data taken prior to and after each test. Due to the presence of

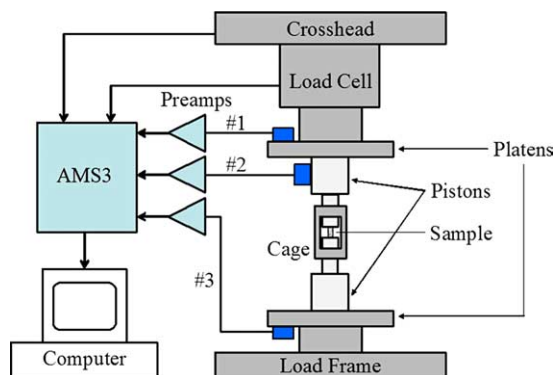


Fig. 3. Schematic diagram illustrating the experimental setup for measurement of foam acoustic and mechanical data.

coupling fluid between the sample faces and pistons, foam samples were subject to some realignment during initial loading, causing the lowest strain data to be inaccurate.

Acoustic activity was measured during compression by three broadband piezoelectric transducers (Deci Model SE9125-M) and recorded after pre-amplification (34 dB) using a Vallen AMS3 acoustic emissions test system (Fig. 3). One transducer (no. 2) was fixed to the upper piston using a rubber o-ring, while the remaining two (nos. 1 and 3) were magnetically fixed to the machine platens. All transducers were coupled using silicone grease. The amplitude detection range was 33.7–99.9 dB relative to a 1 μ V transducer output before pre-amplification, with all events greater than 99.9 dB in amplitude recorded as 99.9 dB. Time resolution and rearm time for all transducers were 0.1 μ s and 3.2 ms, respectively. At each detected event, crosshead displacement and load were simultaneously recorded from the load frame. In order to estimate noise generated by friction in the gauge region (for example, between the aligning sleeve and pistons), acoustic activity was also recorded during motion of the crosshead without the samples, giving a negligible average event rate of 24 (expressed as events per unit macroscopic sample strain, using the gauge length of the amorphous specimen as reference). Frictional noise between foam struts and piston surfaces was estimated using the pure aluminum foam, for which the average event rate was again negligible, 10 per unit strain. Following these tests, it was concluded that extraneous events (i.e. those not originating from inside the foam samples) during compression were negligible relative to the observed event rates, which were on the order of 20,000 in both Vit106 foam samples and 800 in the Al–Si sample.

3. Results and discussion

3.1. Compressive mechanical behavior

Compressive stress–strain curves for the amorphous Vit106, crystalline Vit106, and Al–Si foams are shown in Fig. 4a–c. The amorphous sample (Fig. 4a) exhibited a linear loading region, followed by yield near 27 MPa and a slowly-rising plateau region punctuated by sharp serrations and terminated at high strains by densification, consistent with the general compressive characteristics of other amorphous Vit106 foams of various porosities and pore sizes [14]. Deformation was macroscopically uniform throughout the test without visible crush bands, and the sample was found to be intact (except for minor spalling of material from the edges) after unloading from a final average compressive strain near 80%. By contrast, no quasi-elastic loading region was evident for the crystalline sample (Fig. 4b), and accordingly a yield stress could not be accurately defined. Flow stress was highly uneven throughout the whole strain range and oscillated around a mean value of about 2 MPa, taking a maximum value of 5.5 MPa, well below even the initial yield stress of the amorphous sample. Deformation proceeded by unstable fracture and crushing near the pistons, as indicated by continuous release of numerous sub-millimeter foam fragments from these portions

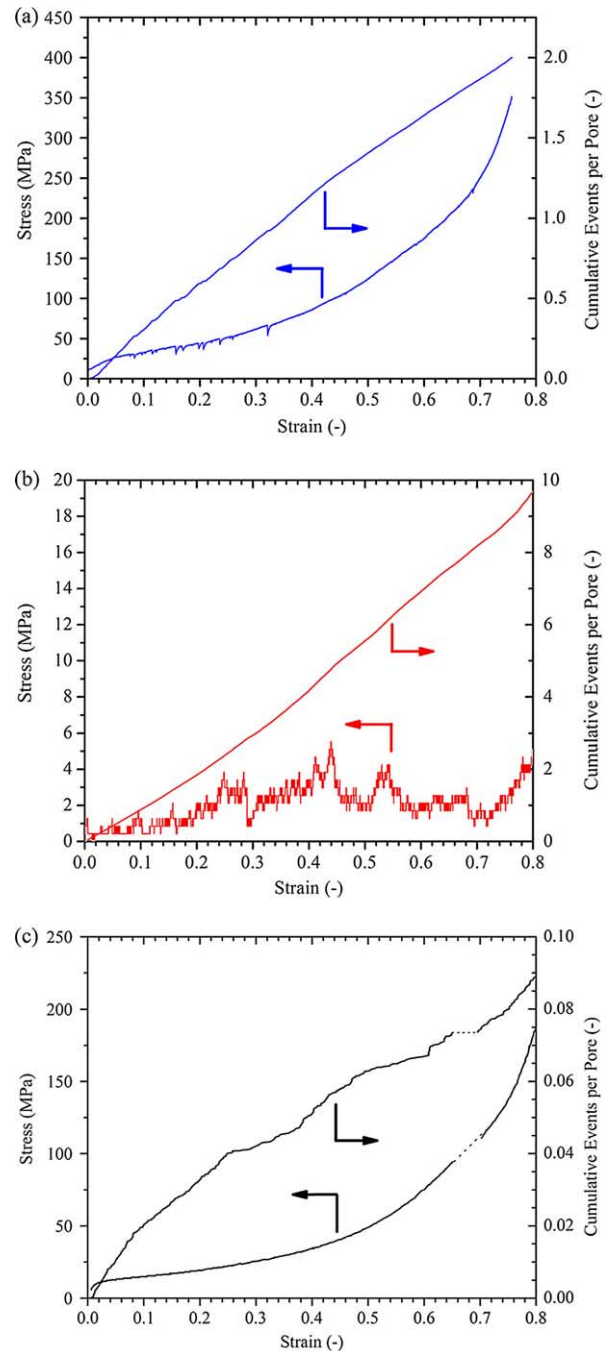


Fig. 4. Compressive stress–strain curves for (a) amorphous Vit106 foam; (b) crystalline Vit106 foam; and (c) eutectic Al–Si foam. Also shown are cumulative AE events, normalized by the estimated number of pores in each sample.

of the sample. Thus, the use of a macroscopic or average strain to describe deformation in this foam is not strictly appropriate, but the term has been retained for simplicity and because of its wide use in literature pertaining even to brittle foam materials. The eutectic Al–Si foam (Fig. 4c) showed linear loading and gradual yielding at stresses in the range of 5–10 MPa, followed by a smoothly increasing plateau region and gradual densification. Deformation of both pure aluminum and eutectic

Al–Si foams was stable and visibly uniform, consistent with prior observations [24], with little noticeable spalling and no evidence of serrations or final fracture in either case.

The total acoustic events generated by the amorphous and crystalline Vit106 foam samples during compression to near 80% nominal strain were approximately 24,800 and 19,200, respectively, while the eutectic Al–Si foam generated only about 650 events over a comparable strain interval and the pure aluminum foam generated negligible acoustic activity, as mentioned previously. Estimating the number of pores in each sample (noting that the pores are generally angular in shape rather than spherical) as the total pore volume $V \cdot p$ (where V is the total sample volume and p the volume fraction of porosity) divided by the pore volume d^3 , where d is the median pore size (180 μm for the amorphous Vit106 and the Al–Si foams and 320 μm for the crystalline Vit106 foam), the total events per pore are estimated as 2.0 for the amorphous and 9.7 for the crystalline Vit106 sample, as shown in Fig. 4a and b. The corresponding value for the Al–Si foam was again much lower, about 0.1 (Fig. 4c). While the exact number of struts per pore depends on foam architecture, it can be stated that a 3D array of cubic cells, each defined by struts comprising its 12 edges and with each such strut shared between four adjacent coplanar cells, has three struts per pore. Thus, it is estimated roughly that during compression to 80% nominal strain the amorphous Vit106 foam exhibited a number of fracture events comparable to, or below, its total number of struts; by contrast, the crystalline Vit106 sample appeared to sustain multiple fractures per strut under the same conditions, and the Al–Si foam showed fracture in only a small proportion of its struts. In interpreting such a result, it is important to recall, however, that direct comparison of event numbers between Vit106 and Al–Si foams may be complicated by differences in internal damping coefficient and transmission properties at the foam/piston interface. The same limitations also apply to direct comparisons of event amplitudes between samples.

3.2. Quantitative AE analysis

Evolution of acoustic activity caused by microfracture within porous solids is often quantified using the concise framework originated by Gutenberg and Richter [25] in their analysis of earthquake magnitudes, a reflection of the view that large-scale (i.e. geological) and small-scale (i.e. microfracture) acoustic events share a common origin in cascades of strain energy release events within self-organized critical (SOC) systems [16,26–28]. The cumulative amplitude distribution of the individual events comprising the cascades of a SOC system takes the form of a power-law; in the case of earthquakes, this is expressed through the Gutenberg–Richter (GR) relationship:

$$\log N(W) = a - b \cdot W \quad (1)$$

where $N(W)$ is the cumulative number of events having magnitude greater than or equal to W and a and b are the seismic GR parameters. Eq. (1) can be applied directly to the analysis of AE data provided that the seismic b parameter is

multiplied by 20 to account for the fact that the amplitude of AE events is recorded in decibels rather than logarithmic peak amplitude; this modified value is referred to as the AE– b parameter [28].

Application of the GR relationship to AE data is widespread in the study of microfracture in rocks [16] and model brittle materials like plaster [26,27] and fiberglass [27], and has been extended successfully to porous brittle solids such as silicate glasses [28,29] and alumina [28]. Its usefulness in these contexts rests on correlation of the GR parameters to internal microfracture mechanisms, and efforts have been directed towards quantitative prediction of the GR parameters in porous brittle solids using material constants influencing microfracture [28]. While quantitative analysis of this sort depends on data that remain unavailable for Vit106, evolution of the GR parameters during foam compression still provides useful insight into the evolution of internal microfracture mechanisms. The GR parameter a in Eq. (1) essentially gives (logarithmically) the total number of AE events in the population. It must be noted, however, that the a parameter represents a hypothetical zero-amplitude intercept for the distribution, while real AE data are truncated by detection thresholds; thus the relationship of a to measured event rate is non-quantitative and in practice may be influenced by the fitted value of AE– b , rendering the latter parameter more reliable. The AE– b parameter quantifies the exponent of decay of the amplitude distribution with increasing amplitude; thus, large values of AE– b reflect AE activity with few high-amplitude fractures, while smaller values of AE– b reflect activity with comparatively more highly-energetic fractures. Values of a vary widely depending on the size of the population being considered and hence are not generally comparable across experiments, but values of AE– b are far more general, with typical values in the range 0.4–2 [28].

Analysis of AE data according to the GR relationship, Eq. (1), was performed for both the amorphous and crystalline Vit106 foam samples as well as the Al–Si foam. In all cases, as well as in the subpopulations discussed later, the distributions showed deviations from Eq. (1) indicative of lower numbers of high-amplitude events than would be predicted by a power-law relationship, as shown in Fig. 5. Deviation at high energies has been noted in other AE studies [26–28,30] and can occur for several reasons. At a fundamental level, it results from the correlation between fracture event energy and the underlying length scale of the associated fracture [16,30]. Power-law behavior in SOC systems is a reflection of self-similarity, and therefore may be expected to persist only to the extent that self-similarity also persists; if an upper limit on fracture length scale (and thus energy) is fixed, for example, by the physical dimension of the sample or proximity to sample surfaces, then a similar limit is imposed on the extent of power-law behavior. Thus deviation of the GR distribution in the region of high event energy may reflect the fact that some events were generated by damage processes having spatial dimensions comparable to those of the sample, or taking place at locations sufficiently close to the sample boundaries that the events become interrupted, in the same way that seismic activity is

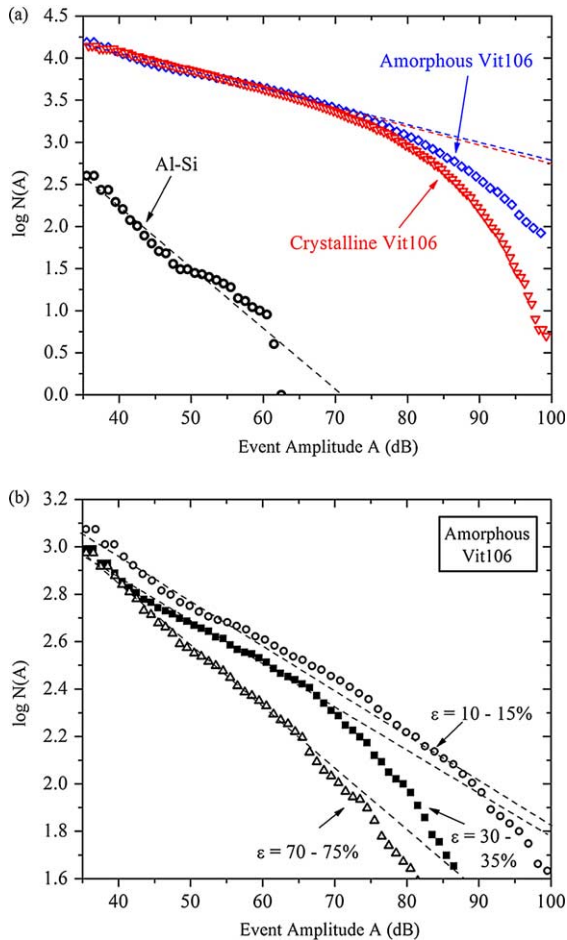


Fig. 5. Cumulative amplitude distributions for AE events studied in this work. (a) Full AE populations from the amorphous and crystalline Vit106 foams and the Al–Si foam. (b) Three subpopulations from the amorphous Vit106 foam, representing the strain intervals 10–15, 30–35 and 70–75%. All distributions show linearity (i.e. power-law scaling) at lower amplitudes with deviation at high-amplitudes. Dashed lines indicate fits using the GR relationship, Eq. (1).

affected by the finite thickness of the seismogenic crust of the earth [16] or model earthquake results deviate due to finite model sizes [30]. Similar power-law deviations may also result if damaged regions begin to impinge and interact, or through saturation effects associated with event counting at high-amplitudes and rates [28,31]. The likelihood of significant high-amplitude events being lost due to hardware saturation effects was low in the present case, however, in light of the fact that high-amplitude deviation was apparent (if less pronounced) in the Al–Si foam despite much lower event rates and a lack of any events approaching the saturation amplitude (99.9 dB). To avoid finite sample size effects and lost events at all values of strain, and to facilitate comparison between Vit106 and Al–Si foams, GR parameters were fitted using data of amplitude < 65 dB.

3.3. General microfracture mechanisms

The value of $AE-b$ obtained by analysis of the entire population of AE events from the amorphous Vit106 foam (whose amplitude distribution appears in Fig. 5a) was

0.42 ± 0.01 , near the lower bound of commonly-observed $AE-b$ values [28]. Low values of $AE-b$ indicate a slow decay of the amplitude distribution, i.e. a broad underlying distribution of fracture energies. That such a broad distribution should exist in the Vit106 foam is not immediately apparent, in light of the fact that amorphous metals typically show little strength variation in monolithic form. However, it has been noted elsewhere [14] that Vit106 struts within a foam fail both uniaxially and in bending, allowing (due to tensile–compressive asymmetry) for strut strengths anywhere between the tensile and compressive uniaxial strengths (1200 and 1800 MPa for Vit106, respectively). This natural distribution, combined with the inherent distribution of strut dimensions in any foam architecture, contributed to the low measured value of $AE-b$ in the amorphous foam.

The value of $AE-b$ measured in the crystalline Vit106 foam (Fig. 5a) was nearly identical, 0.44 ± 0.03 , indicating an equally broad strength distribution (though, as noted above, the absolute amplitudes or strut strengths are not generally comparable between samples). The source of strength distribution in the crystalline sample is the large fraction of brittle intermetallics phases resulting from the devitrification treatment, which, unlike the pure amorphous phase, are subject to natural strength statistics as well as substantial tensile–compressive asymmetry. A similar interpretation applies to the relationship between $AE-b$ values in amorphous Vit106 foam and those measured in other highly-porous brittle ceramics expected to show strength-scaling or Weibull behavior. In glassy SiO_2 having relative density 28–32%, $AE-b$ values were found to lie in the range 0.38–0.63, while in Al_2O_3 of relative density 29–31% the range was 0.34–0.52, both comparable to the measured values in Vit106 [28].

According to such an explanation, the narrower strength distribution among more ductile Al–Si struts (which show little or no tensile–compressive asymmetry) should lead to a narrower distribution in amplitude distribution, i.e. to a higher value of $AE-b$. Indeed, the value of $AE-b$ for the Al–Si foam, 1.44 ± 0.08 , was significantly above the values characterizing the Vit106 and ceramic foams (Fig. 5a) [28]. This higher degree of uniformity should allow for more gradual and diffuse damage accumulation by allowing fractures to nucleate more uniformly within the structure and by diminishing the number of anomalously-strong struts whose failure might initiate a localized damage cascade in the surrounding material. Consequently, it is suggested that high $AE-b$ values (i.e. damage dominated by low-energy failures, such as in the Al–Si) represent diffuse damage accumulation, while lower $AE-b$ values reflect a higher degree of damage localization. Such a conclusion is in line with observations from the brittle ceramic foams described above; in these systems, higher values of $AE-b$ were found in weaker samples that showed some gradual damage accumulation, while stronger samples with lower $AE-b$ failed more catastrophically [28]. From this standpoint the difference in $AE-b$ between ductile Al–Si foam and the more brittle Vit106 and ceramic foams reflects a greater tendency towards damage localization in the latter, a process that in many cases foreshadows final failure.

3.4. Damage evolution

In order to quantify evolution of the internal damage process during compression of the amorphous Vit106 foam, and thereby identify the strains at which the predicted damage localization may be occurring, AE data were separated into subpopulations representing 5% intervals of applied strain and the cumulative amplitude distribution of each subpopulation was fitted to the GR relationship, Eq. (1). Three such distributions, corresponding to three different 5% strain intervals, are shown in Fig. 5b to highlight variations in $AE-b$, i.e. in the slope of the low-amplitude region of the distributions. Similar analysis using the Al-Si foam was, unfortunately, not possible because the low event rate in this sample did not permit statistically-reliable conclusions to be made using comparable subpopulations.

Evolution of the total events in each interval and the $AE-b$ parameter for amorphous Vit106 foam are shown in Fig. 6 as functions of applied strain, with macroscopic yield indicated by the dashed lines. As shown in Fig. 6a, the measured events in each 5% strain interval decreased from a maximum just after

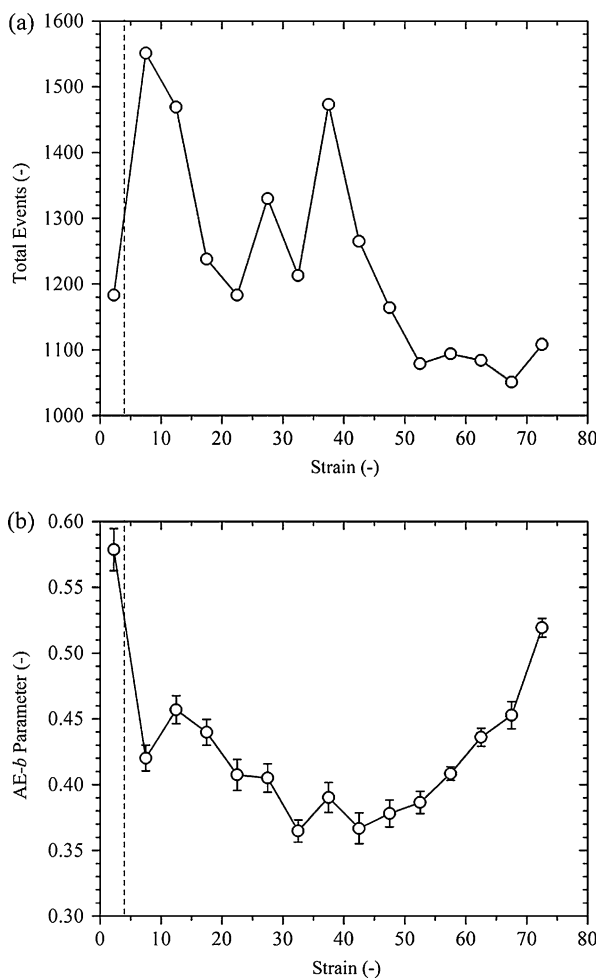


Fig. 6. Evolution of acoustic activity in amorphous Vit106 foam with increasing applied strain, in 5% intervals. (a) Total events in each interval; (b) the GR parameter $AE-b$ characterizing each interval. Yield is indicated in both plots by vertical dashed lines.

yield through the densification region, albeit with large variations in the early plateau region. This behavior is generally consistent with a weakest-link mechanism in which fracture occurs first in the (large) population of features having low or average strength, and tending at higher strain towards sampling of the (smaller) high-strength tail of the strength distribution, with large variations likely resulting from the occasional generation of intense localized damage (as described below). A similar but more stable trend was evident for $AE-b$ at low and intermediate strains, but whereas event rates continued falling within the densification region, the amplitude distribution of these events reverted towards higher $AE-b$ (Fig. 6b) at the highest strains.

Progression of the fracture mechanism from high $AE-b$ values in the quasi-elastic loading region towards lower $AE-b$ after significant deformation indicates an underlying evolution of the microfracture process from one consisting of primarily low-energy fractures towards one consisting of a greater proportion of energetic fractures. In keeping with the interpretation of the previous paragraph, this corresponds to sampling primarily of the (large) population of weaker struts at low strain, with a gradual evolution towards sampling of the (smaller) population of strong struts as well (note that power-law scaling ensures that the total events, Fig. 6a, are always dominated by low-energy fractures and hence do not reflect this trend as clearly). Similarly, reversal of the trend at the highest strains (60–75%) indicates evolution back towards fewer (Fig. 6a) and less energetic (Fig. 6b) strut fractures, probably reflecting both exhaustion of the strongest portion of the strut population and the increasing effects of confinement associated with densification. Geometric confinement is known to increase ductility in amorphous metals, and might therefore have imparted improved fracture resistance to any struts surviving intact to such high strains [32,33].

For the reasons given in the previous section, it is further concluded that intervals of strain characterized by high $AE-b$ values (i.e. dominated by these weaker failures) represent diffuse damage accumulation, while those intervals showing higher $AE-b$ reflect instances of damage localization. Thus the early progression of damage was from diffuse to localized damage, a familiar progression in materials or systems failing by a weakest-link mechanism; however, unlike most such systems, the Vit106 foam did not fail catastrophically upon failure of its strongest components, but rather reversed course towards diffuse damage again. The mechanism of this reversal is rationalized easily through the effects of confinement, but it remains noteworthy that the foam maintained integrity long enough for confinement effects to come into play. Its ability to do so (where, by comparison, comparable SiO_2 and Al_2O_3 foams failed at much lower strains despite having nearly identical AE signatures [28]) indicates that even severe and relatively localized damage events could be accommodated by the structure without overall failure, an ability that derives not only from the presence of a restraining network of ductile struts but also from a stabilizing mechanism associated with the foam structure itself.

Accommodation of the fracture of brittle struts in amorphous Vit106 foam by the surrounding networks of ductile struts was facilitated by the formation of point contacts between the enlarged nodes that connect struts within the replicated foam structure (Fig. 2). These large nodes, which are characteristic of replicated foam structures due to the irregularity of salt particle packing [19,23], were brought into contact with struts and neighboring nodes at relatively low local strains and thereby limited the severity of local pore collapse that would normally accompany energetic strut failures. In doing so, they also minimized the destabilizing effects that collapse of a pore would exert on neighboring struts, damping the propagation of large spatially-limited cascades of pore failure that are often manifested in cellular materials as crush bands or macrocracking. Additional evidence of the importance of such contact forces within replicated amorphous Vit106 foam takes the form of early increases in reloading stiffness (which in the absence of such forces should decrease rapidly until final densification in response to microfracture damage) after low strains of only 5–10% after yield, by the rapid increase of flow stress throughout the plateau region, and by a lack of visual evidence for large-scale crush bands during deformation [14], all of which were also observed to some degree in replicated aluminum foam [23,24]. The existence of such mechanisms is believed to explain the ability of the amorphous Vit106 foam to undergo periods of localized fracture similar in every way to those seen in brittle crystalline Vit106 and ceramic foams, without the macroscopic failure observed in those cases. The details of how such localized damage was nucleated and damped in the amorphous Vit106 foam is considered in Section 3.5.

3.5. Stress serrations

A distinguishing feature of amorphous Vit106 foam deformation is the presence of visible serrations in the plateau region of the stress–strain curve (Figs. 4a and 7), which have

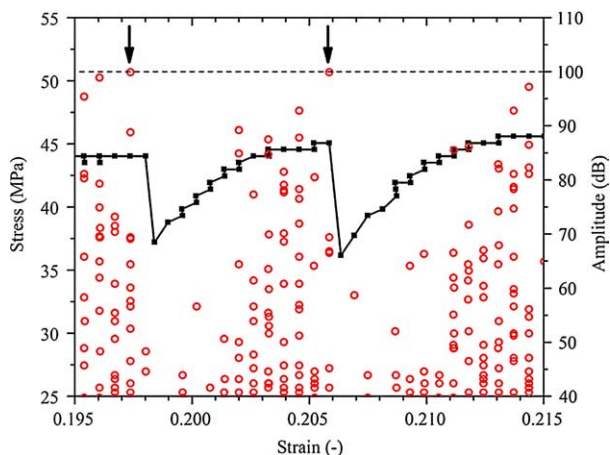


Fig. 7. Strain dependence of acoustic event amplitude (open circles, right scale) and stress (solid squares and line, left scale) in a region with two stress serrations, showing high-energy events initiating the serrations (indicated by arrows; the horizontal dashed line shows the hardware saturation limit), followed by decreased acoustic activity during stress recovery.

been reported for a range of Vit106 foams and whose variation with relative density and pore size can be explained in terms of foam architecture and the underlying mechanics of ductility in amorphous metal foam struts [14]. These serrations, which were present in neither the pure aluminum nor Al–Si foam, clearly represent large damage events of the sort discussed previously, but it is unclear from stress–strain data alone whether the underlying process involved a single (or few) highly energetic fractures or the cooperative fracture of many struts involved in a diffuse cascade, and to what extent (if any) these serrations are indicative of crush band nucleation. Both issues may be approached through GR analysis, as described below.

To isolate fracture processes preceding major serrations (i.e. serrations involving a relative loss in flow stress of 5% or more, of which there were twelve in the amorphous foam; no distinct serrations could be identified in the crystalline foam due to highly irregular flow stresses everywhere), the population consisting of the last 100 AE events preceding each serration was analyzed. The average event rate during these periods was elevated, ca. 33,000 per unit strain compared to an average of 25,000 for the entire test, and the parameter $AE-b$ for the pre-serration population took the value 0.53 ± 0.05 . Since serrations were quite uniformly distributed within the region of low $AE-b$ shown in Fig. 6b (the first and last serrations occurred around 7.5 and 32.1% strain, Fig. 4a), and since this value of $AE-b$ was significantly higher than any of the values in that region (the highest of which was 0.46 ± 0.01), this result is not simply an artifact of the larger evolution of behavior described in Section 3.4. The results indicate instead that immediately prior to the major serrations, the microfracture process consisted of a large number of relatively low-energy fractures. Such behavior can be interpreted as the accumulation of diffuse damage, in which the concentration of small damaged sites increases with strain until several such sites suddenly link, causing a macroscopic damage event, visible as a serration on the stress–strain curve. As described above, the constraining network of ductile struts and the formation of contact forces during such events prevented immediate sample failure at the serrations, though flow stress recovery was not immediate.

The last event recorded before each serration stress drop was typically of very high-amplitude: of the 12 serrations considered, 11 were immediately preceded by a saturating event of 99.9 dB (arrows in Fig. 7). Over the full course of the compression test, however, there were a total of 62 additional saturating events that did not precede any visible serrations. This suggests the observable serrations may have had actual amplitudes well in excess of that required to cause saturation in the acquisition hardware, and is in keeping with visual evidence of sparks accompanying serrations [14]. Still, the average of the five events preceding each of the serrations was only 49 dB, so that the immediate source of serrations was the highly energetic fracture of a single strut or small number of struts, as compared to the collective fracture of a large number of weaker struts such as characterized the pre-serration periods. Therefore, linking of the smaller damage sites produced during

the pre-serration periods into a single macroscopic flaw was ultimately restricted by the persistence of a single (or small number of) strong ligaments, and serrations resulted from the sudden failure of these ligaments and corresponding collapse of the surrounding regions of diffuse damage. Collapse produced sudden samples deflections that become manifested as stress drops during displacement-controlled compression tests.

Interpretation of stress serrations as indicative of damage localization is consistent with AE observations in Bentheim sandstone (porosity 22.8%), which showed similar behavior defined by short bursts of AE activity concurrent with stress serrations in an otherwise increasing stress–strain curve [34]. Micrographic analysis of these sandstones clearly showed formation of discrete and large-scale compaction bands resembling the crush bands common to metallic foams. Whether the localized damage regions in amorphous Vit106 foam followed conventional crush banding behavior, in the sense of radiating uniformly into the gauge length from a single source band, or whether serrations corresponded to formation of distinct bands in separate regions of the gauge length, is unclear from the AE data. Clarification could be offered by spatial localization of AE events using triangulation techniques or by microtomographic reconstruction of the foam at various stages of deformation.

Events recorded during the periods of stress recovery following each stress drop were generally low in magnitude and were characterized by an $AE-b$ value of 0.47 ± 0.01 . This value was higher than the overall values characterizing the early plateau region where the serrations occurred (Fig. 6b), indicating a fairly low-energy fracture process during recovery. Event rates during recovery were less than the overall average event rate by a factor of three, as exemplified by plotting AE events alongside a small serrated portion of the stress–strain curve (Fig. 7). However, these rates were still well above any of the noise levels observed in other tests, and more than a factor of three higher than event rates measured during deliberate unloading/reloading cycles not following serrations. Since the Kaiser effect, i.e. the cessation of acoustic activity during unloading and reloading at stresses below that from which the material was unloaded, has been near-perfectly represented in monolithic amorphous metals [35,36], this AE activity during recovery was likely the combined result of small numbers of strut fractures resulting from redistribution of internal stresses, as well as frictional noise generated between recently broken foam features. Frictional events may have been especially numerous during recovery due to the large number of contacts formed during localized collapse at the serration, and the relatively large strut reorientations that likely accompanied stress redistribution. Accordingly, it is concluded that some accommodation certainly took place in the foam during recovery from large fracture events; these accommodation events were independent, however, of the immediate mechanism by which the initial high-energy fracture cascade was terminated, since AE events during recovery occurred only after comparatively large intervals of time and strain following the stress drop. This result is consistent with the view that

additional mechanisms besides fracture (e.g. plasticity in nearby ductile struts, and the formation of new internal contacts) were responsible for preventing final failure in the amorphous foam.

4. Conclusions

Due to their high compressive ductility and density-compensated strength, amorphous metal foams show considerable promise as lightweight structural materials and may eventually find application as structural paneling, energy-absorbing structures, or even orthopedic biomaterials [6,13]. In all such applications, fundamental understanding of underlying deformation mechanisms is essential to safe and efficient use, but much of this understanding is still lacking for amorphous metal foams, which exhibit a complex combination of ductile and brittle strut deformation mechanisms.

In this report, acoustic emissions were analyzed to probe internal deformation in low-density open-celled amorphous metal foams processed from a commercial glass-forming alloy using a salt replication method, and to contrast this deformation against parallel mechanisms operating in brittle (crystalline Vit106) and ductile (eutectic Al–Si) foams of the same architecture. Based on analysis of acoustic data within the Gutenberg–Richter framework, a mechanism of deformation was proposed for amorphous Vit106 foams, in which diffuse low-energy fracture progresses into localized collapse and recovery at intermediate strains, and finally into diffuse damage due to confinement at the highest strains. Cell collapse associated with microfracture damage linkup in the intermediate strain region was stabilized by a constraining network of ductile struts and by the formation of point contacts, such that even these large damage events could be accommodated without catastrophic sample failure. The existence of these mechanisms provides an explanation for how amorphous metal foams exhibit compressive behavior similar to ductile crystalline metal foams, while sustaining internal damage on par with brittle ceramic foams.

Acknowledgements

The authors acknowledge the financial support of the DARPA Structural Amorphous Metals Program (ARO Contract No. DAAD 19-01-1-0525) and thank the Caltech Center for Structural Amorphous Metals for providing supplies and facilities to arc-melt Vit106 buttons. The authors also thank Dr C. San Marchi (currently at Sandia National Laboratories, Livermore, CA) for his assistance during the early stages of the project and for fabrication of the pure aluminum foam used to investigate frictional noise levels.

References

- [1] Ashby MF, Evans AG, Fleck NA, Gibson LJ, Hutchinson JW, Wadley HNG. *Metal foams: a design guide*. Boston: Butterworth-Heinemann; 2000.
- [2] Banhart J. *Prog Mater Sci* 2001;46:559.
- [3] Johnson WL. *JOM* 200240.

- [4] Inoue A, Shen BL, Koshiba H, Kato H, Yavari AR. *Acta Mater* 2004;52:1631.
- [5] Schroers J, Veazey C, Demetriou MD, Johnson WL. *J Appl Phys* 2004;96:7723.
- [6] Brothers AH, Dunand DC. *Scripta Mater* 2006;54:513.
- [7] Conner RD, Li Y, Nix WD, Johnson WL. *Acta Mater* 2004;52:2429.
- [8] Lee JC, Kim YC, Ahn JP, Kim HS. *Acta Mater* 2006;54:513.
- [9] Schroers J, Johnson WL. *Phys Rev Lett* 2004;93.
- [10] Wada T, Inoue A, Greer AL. *Appl Phys Lett* 2005;86:251907.
- [11] Wada T, Inoue A. *Mater Trans* 2003;44:2228.
- [12] Wada T, Inoue A. *Mater Trans* 2004;45:2761.
- [13] Brothers AH, Dunand DC. *Adv Mater* 2005;17:484.
- [14] Brothers AH, Dunand DC. *Acta Mater* 2005;53:4427.
- [15] Clyne TW, Withers PJ. *An introduction to metal matrix composites*. New York: Cambridge University Press; 1993.
- [16] Hatton CG, Main IG, Meredith PG. *J Struct Geol* 1993;15:1485.
- [17] Knehans R, Steinbrech R, Schaarwachter W. *Mater Sci Eng* 1983;61:17.
- [18] Kadar C, Chmelik F, Rajkovits Z, Lendvai J. *J Alloys Compd* 2004;378:145.
- [19] Brothers AH, Scheunemann R, DeFouw JD, Dunand DC. *Scripta Mater* 2005;52:335.
- [20] Conner RD. Personal communication; 2003.
- [21] Mukherjee S, Zhou Z, Schroers J, Johnson WL, Rhim WK. *Appl Phys Lett* 2004;84:5010.
- [22] San Marchi C, Mortensen A. In Degischer H.P. Kriszt B. editors. *Handbook of cellular metals: production, processing, applications*. Weinheim: Wiley-VCH; 2002 [chapter. 2].
- [23] San Marchi C, Mortensen A. *Acta Mater* 2001;49:3959.
- [24] San Marchi C, Despois JF, Mortensen A. *Acta Mater* 2004;52:2895.
- [25] Gutenberg B, Richter CF. *Bull Seismol Soc Am* 1942;32:163.
- [26] Petri A, Paparo G, Vespignani A, Alippi A, Costantini M. *Phys Rev Lett* 1994;73:3423.
- [27] Garcimartin A, Guarino A, Bellon L, Ciliberto S. *Phys Rev Lett* 1997;79:3202.
- [28] Aue J, De Hosson JTM. *J Mater Sci* 1998;33:5455.
- [29] Maes C, Van Moffaert A, Frederix H, Strauven H. *Phys Rev B* 1998;57:4987.
- [30] Chen K, Bak P, Obukhov SP. *Phys Rev A* 1991;43:625.
- [31] Okoroafor EU, Hill R. *J Mater Sci* 1995;30:4233.
- [32] Yokoyama Y, Inoue K, Fukaura K. *Mater Trans* 2002;43:3199.
- [33] Conner RD, Johnson WL, Paton NE, Nix WD. *J Appl Phys* 2003;94:904.
- [34] Baud P, Klein E, Wong TF. *J Struct Geol* 2004;26:603.
- [35] Bakai AS, Bakai SA, Mikhailovskii IM, Neklyudov IM, Stoev PI, Macht MP. *Jetp Lett+* 2002;76:218.
- [36] Vinogradov AY, Khonik VA. *Philos Mag* 2004;84:2147.